An idealized modeling study of nocturnal cooling processes inside a small enclosed basin

M. T. Kiefer[1] and S. Zhong[1]

Received 15 April 2011; revised 15 August 2011; accepted 15 August 2011; published 28 October 2011.

[1] The Advanced Regional Prediction System is utilized to examine the evolution of the nocturnal boundary layer observed within Arizona's Meteor Crater, a small enclosed basin, on quiescent nights during the 2006 Meteor Crater Experiment field campaign. Two aspects of the observed basin atmosphere are investigated: a quasi steady-state three-layer temperature structure, including an isothermal layer away from the basin floor, and the intrusion of a regional-scale cold air drainage flow into the basin. In general, the two-dimensional numerical simulations are able to reproduce the salient features of the nocturnal boundary layer inside Meteor Crater. A combination of increasingly cold air intruding into the basin and pooling near the basin floor and compensating adiabatic ascent yield an isothermal layer over a large depth of the basin atmosphere. A series of experiments are then conducted in order to examine the sensitivity of basin thermal structure to upstream terrain slope, basin width, and the presence of a rim surrounding the basin. In the case of a large basin of O(10 km) in diameter, the cold air intrusion process remains, but the larger basin volume yields greater dilution of the cold air intruding into the basin, and a weak inversion develops inside the basin away from the floor. In the case of a small basin with the same dimensions as Meteor Crater but with flat upstream terrain, the influence of the surrounding terrain on basin cooling is negligible. Last, the presence of a rim surrounding the basin is found to not be necessary for isothermal layer development.

Citation: Kiefer, M. T., and S. Zhong (2011), An idealized modeling study of nocturnal cooling processes inside a small enclosed basin, *J. Geophys. Res.*, *116*, D20127, doi:10.1029/2011JD016119.

1. Introduction

[2] The development and evolution of nocturnal boundary layers within mountain basins is a subject of great interest to researchers studying, for example, air pollution in basins [*Reddy et al.*, 1995] and aviation impacts from reduced visibility [*Smith et al.*, 1997]. A common feature of nocturnal boundary layers in basins are cold air pools, defined as topographically confined, stagnant layers of air that are colder than the overlying air [*Whiteman et al.*, 2001]. In extreme cases, the air temperature near the surface in valleys or basins may be on the order of 10 K colder than near-surface air over the adjacent plain [*Whiteman et al.*, 2001]. Further, cold air pools may be categorized as diurnal [e.g., *Whiteman et al.*, 1996; *Clements et al.*, 2003] or persistent [e.g., *Whiteman et al.*, 2001; *Steinacker et al.*, 2007], based on the duration of the event. In this study our focus is on the former. The accepted theory on diurnal cold air pool formation in valleys and basins [*Geiger*, 1965] dictates that radiation loss along sloping terrain drives a downslope flow of cold air into the developing cold air pool, amplifying the cooling occurring due to radiative heat loss at the valley or basin floor. A number of observational studies have examined such slope flows and have generally confirmed the importance of such flows in cooling of the near-surface air in valleys [e.g., *Barr and Orgill*, 1989; *Mahrt et al.*, 2001; *LeMone et al.*, 2003].

[3] Cold-air pools have also been shown to form in situ in valleys or basins in the absence of drainage flow [*Thompson*, 1986]. Cooling of the basin atmosphere in the absence of drainage flow may occur through turbulent heat flux divergence, radiative flux divergence, or a combination of the two processes. *Clements et al.* [2003] found that a cold air pool in the Peter Sinks basin of Utah during September 1999 formed in situ, mainly the result of radiative flux divergence following a 1.5 h period near sunset in which turbulent flux divergence dominated the surface cooling. In contrast, modeling studies such as *Vosper and Brown* [2008] and observational studies such as *Gustavsson et al.* [1998] point to turbulent heat flux divergence as being the primary source of basin atmosphere cooling, wherein the sheltering effect of a valley or basin leads to a reduction of turbulent fluxes above the surface (e.g., 10 m above ground level). The result of such sheltering is rapid basin cooling since the

[1]Department of Geography, Michigan State University, East Lansing, Michigan, USA.

0148-0227/11/2011JD016119

downward sensible heat flux at the surface is not matched by a downward turbulent heat flux in the atmosphere above the surface. Thus net surface cooling is greater within the valley or basin than elsewhere.

[4] An improved understanding of the physical processes governing the evolution of cold air pools was a primary motivation for the Meteor Crater Experiment (METCRAX) conducted during October 2006 within Arizona's Meteor Crater near Winslow, Arizona [*Whiteman et al.*, 2008]. While other field studies have contributed to our understanding of stable boundary layer structure and evolution in valleys and basins [e.g., *Whiteman et al.*, 1999; *Clements et al.*, 2003; *Steinacker et al.*, 2007], the METCRAX experiment was unique in terms of the idealized nature of the study area. Meteor Crater, being symmetrical in shape and exhibiting uniform slope and sidewall heights without gaps, made it an ideal site for examining boundary layer growth and evolution. The crater, formed approximately 50,000 years ago by a meteorite impact, is approximately 165 m deep and 1200 m in diameter at rim level. The rim of the crater rises approximately 50 m above the surrounding plain and is unbroken by large saddles or passes.

[5] During the experiment, a large number of continuous observations were made from in situ and remote sensing instruments inside and outside the crater. Continuous measurements of mean meteorological variables, turbulence fluxes, and radiative and soil fluxes were made inside the crater using an array of Integrated Surface Flux Facility (ISFF) towers. In addition, vertical profiles of mean meteorological variables through the depth of the crater atmosphere were made during intensive observational periods, chosen on the basis of forecasts of quiescent synoptic conditions favorable for formation of cold air pools, gravity waves, and seiches. For further details about the instrumentation and quality control of data collected during METCRAX, the reader is referred to *Whiteman et al.* [2008] and *Yao and Zhong* [2009]. The topography of Meteor Crater, along with locations of tethersonde sites within the crater basin and the rawinsonde site located north-northwest of Meteor Crater, is presented in Figures 1a and 1b.

[6] The METCRAX data revealed a nocturnal boundary layer structure that is unique to the crater or small enclosed basin [*Whiteman et al.*, 2008]. Unlike the nocturnal boundary layer over flat terrain or inside a large basin that is generally characterized by an increase of temperature with height, the crater boundary layer shows a three-layer structure that consists of a strong surface inversion, an overlying nearly isothermal layer, and a secondary inversion near the top of the crater basin. Such a structure had not been observed in prior studies of nocturnal boundary layer structures in closed basins [e.g., *Clements et al.*, 2003; *Steinacker et al.*, 2007], although broadly similar structures inside confined valleys have been simulated previously [e.g., *McNider and Pielke*, 1984]. In addition to the three-layer structure, a horizontally homogeneous state was observed away from the basin floor and the sidewalls, as evidenced by nearly identical profiles measured simultaneously at three sites spanning the crater [*Whiteman et al.*, 2008]. Extensive evidence of the unique atmosphere inside Meteor Crater may be found in the work of *Whiteman et al.* [2008, 2010]. As an example, the three-layer horizontally homogeneous atmosphere observed inside Meteor Crater during the intense observational period 5 (22–23 October 2006) is presented in Figure 1c. In general, the three-layer thermal structure and horizontal homogeneity were restricted to quiescent nights, where the term "quiescent" refers here to a lack of synoptic-scale phenomena (e.g., fronts, cyclones) along with surface winds outside the basin generally less than 5 m s^{-1} [*Yao and Zhong*, 2009].

[7] Another phenomenon observed during METCRAX was the persistent intrusion of a regional-scale cold air drainage flow into the crater basin [*Whiteman et al.*, 2010]. Such terrain-induced flows are common in regions of complex topography, such as the area surrounding Meteor Crater, and may occur on local or regional scales [*Savage et al.*, 2008]. Meteor Crater is situated in an area of gradually sloping terrain of approximately 2% slope, with higher terrain located west-southwest of the crater basin (Figure 1a); the slope is approximately homogeneous over an 80 km long distance. The cold air intrusion phenomenon was first identified by *Whiteman et al.* [2010] and was suggested therein as the cause of the isothermal layer. *Whiteman et al.* [2010] also proposed specific atmospheric processes that could be responsible for the unique three-layer structure, including detrainment of cold air from the inflow layer along the basin sidewall, adiabatic cooling of the basin atmosphere, and continual cooling of the air intruding into the basin. These physical processes were tested with an analytical model by *Haiden et al.* [2011], with the modeling results affirming the likely role of each of the processes in the isothermal layer development. These processes will be examined in detail in section 3. In contrast, understanding of the role of the rim surrounding the crater basin on the nocturnal cooling process is rather limited; however, recent studies have begun to examine the subject, suggesting deflection of regional drainage flow [*Whiteman et al.*, 2010] and the generation of turbulence near the top of the basin cold air pool [*Fritts et al.*, 2010] as possible rim impacts. It is important, however, to emphasize the nearly idealized nature of Meteor Crater, with a minimal impact on nocturnal basin cooling from large-scale advection and flow through saddles or passes.

[8] This paper examines the sensitivity of basin cooling processes and resultant thermal structure inside Meteor Crater to a number of factors that prior research suggests may be critical, including basin size, background terrain slope, and the presence of a rim or lip surrounding the basin. A modeling study of this nature requires simultaneously modeling small-scale terrain features (e.g., a basin rim), which requires fine vertical and horizontal model resolution, and the development of regional-scale drainage flow, which necessitates a model domain of O(10 km) or greater. Such requirements combined with the need to run multiple simulations for each parameter (e.g., basin size) was the primary reason behind the decision to perform only two-dimensional simulations. Limitations of the 2-D model framework will be discussed later in the paper. The remainder of this paper is organized as follows. A description of the numerical model used in this study and the experiment design are presented in section 2. Results and discussion of the

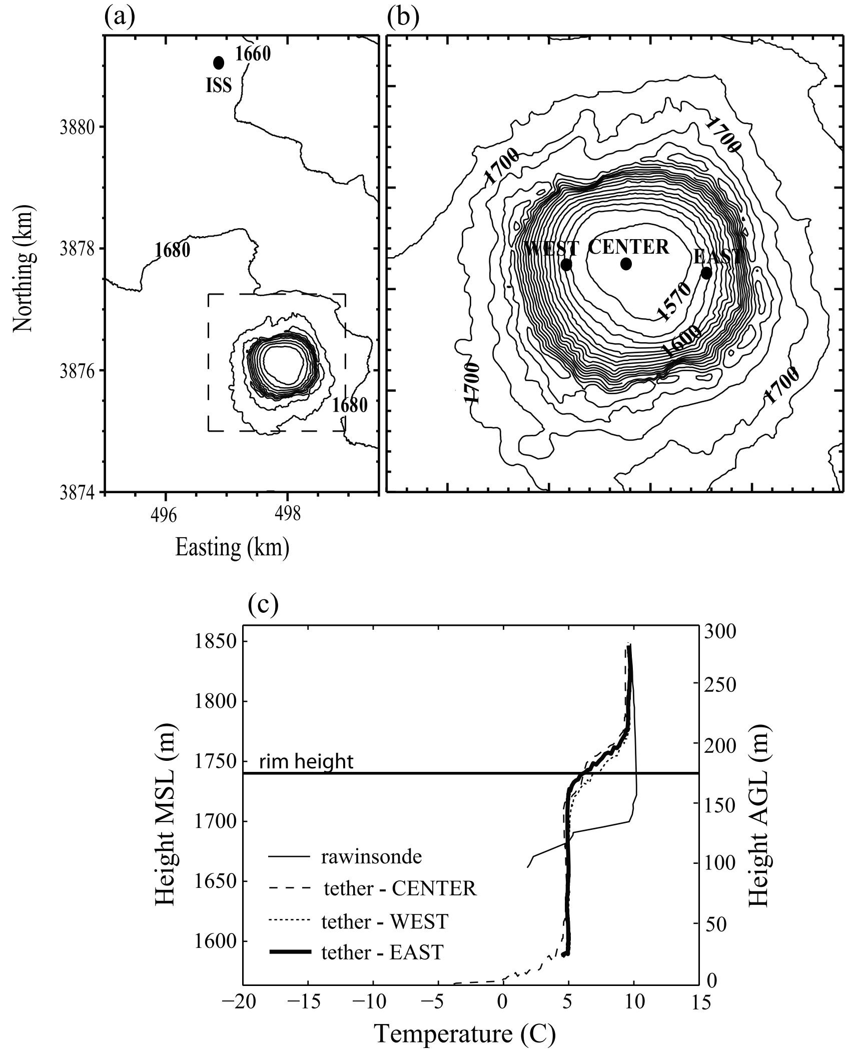

Figure 1. (a and b) Topographic map of Arizona's Meteor Crater. Figure 1b is a zoomed-in view of the inset region indicated in Figure 1a by the dashed outline. Contour interval in Figure 1a is 20 m and in Figure 1b is 10 m. Adapted from *Yao and Zhong* [2009]. (c) Coincident temperature soundings made from the east lower slope ("east" in Figure 1b), central floor ("center" in Figure 1b), and west lower slope ("west" in Figure 1b) tethersondes inside the crater and the rawindsonde (ISS in Figure 1a) outside the crater at 0308 MST 23 October 2006, during Meteor Crater Experiment (METCRAX) intensive observational period 5. For reference, astronomical sunset occurred at 1738 MST 22 October, although local sunset varies depending on location within the basin (local sunset at basin center was 1606 MST). Elevation of the crater rim is indicated by a horizontal line.

experiments are presented in section 3, and the paper is concluded in section 4.

2. Model Description and Experiment Design

[9] The numerical model utilized for this study is the Advanced Regional Prediction System (ARPS) Version 5.2.7 [*Xue et al.*, 2000, 2003]. ARPS is a three-dimensional, compressible, nonhydrostatic atmospheric modeling system with a terrain-following coordinate system. A 1.5-order subgrid-scale turbulence closure scheme with a prognostic equation for the turbulent kinetic energy is utilized, as well as a land surface and vegetation model based on *Noilhan and Planton* [1989] and *Pleim and Xiu* [1995] and radiation physics following *Chou* [1990, 1992] and *Chou and Suarez* [1994]. Effects of topographic shading on radiative fluxes are accounted for as in the work of *Colette et al.* [2003]. Fourth-order accurate finite differencing of the advection terms is used in both the vertical and horizontal directions, while the upper boundary condition for all simulations is a sponge layer extending from z = 6.1 km to the model top at z = 8 km. Owing to the regional-scale domain size, the Coriolis force is computed (as a function of central latitude only). However, moist processes are omitted in all simulations and the sounding utilized is completely dry.

[10] A two-dimensional computational domain has been utilized in this study in order to meet the competing demands of fine resolution required inside the basin and the large domain size needed to allow a mature regional-scale

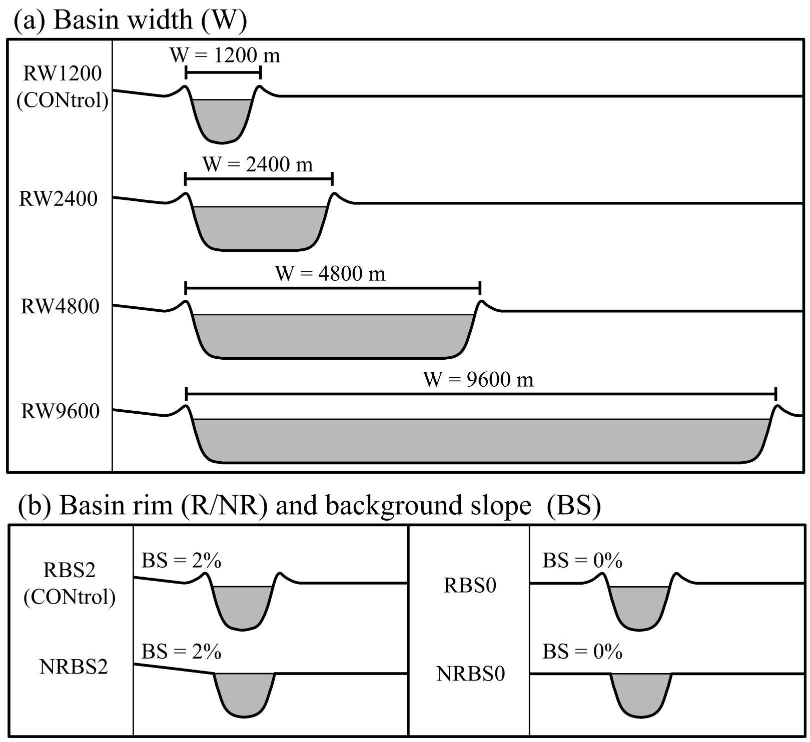

Figure 2. Summary of numerical experiments. For all experiments, the western edge of the basin is located 30 km downstream of the western lateral boundary, with the eastern edge of the basin located a minimum of 20 km from the eastern lateral boundary; only a subset of the domain focused on the basin itself is displayed. Note that the control case, denoted CON, may alternately be referred to as RW1200 or RBS2. For simplicity, the name CON will be used throughout this paper. Gray shading depicts the area utilized for computing basin cooling rate in sections 3.2 and 3.3.

drainage flow to develop. To accurately represent local forcing within the region of the basin, 30-m horizontal grid spacing is utilized along with a vertically stretched grid with minimum vertical grid spacing of 2.5 m near the surface. The grid is gradually stretched to 300 m at the model top. The model domain, which is centered at 35.028 N, −111.023 W (the coordinates of Meteor Crater), extends 60 km in the x direction and 8 km in the z direction. Experiments in which horizontal and vertical domain sizes were allowed to vary indicate that the horizontal domain is sufficiently large to allow drainage flows to fully develop, while further increasing the vertical domain size has negligible impacts on model results (not shown). Orlanski-type open lateral boundary conditions are utilized, with the western lateral boundary located 30 km from the western edge of the basin and the eastern lateral boundary located a minimum of 20 km from the eastern edge of the basin.

[11] For all simulations, ARPS has a horizontally homogeneous initial condition. A base state sounding consisting of a uniform 2 m s^{-1} westerly wind and neutral static stability is utilized for all experiments. Such an initial state is chosen to allow the study to focus on nocturnal cooling processes under generally quiescent conditions, without additional complications such as vertically propagating gravity waves or turbulence generated due to strong flow over the basin rim. It should be emphasized that the 2 m s^{-1} wind speed represents background conditions well away from the basin and is not meant to represent regional drainage flow, which is allowed to naturally develop in the model as the upstream sloped terrain cools via radiative loss. The model is initialized approximately 1 h before local sunset and is run for a total of 6 h to simulate the development of the nocturnal cold air pool. The radiation model utilizes a lookup table for shortwave radiation values corresponding to the late October period, while longwave radiative components are computed as a function of the evolving surface and air potential temperature. Thus the overall experiment design is intended to represent background conditions during quiescent periods of the METCRAX campaign but not any specific case.

[12] Two sets of experiments are conducted in this study: experiments wherein basin size is varied (as measured by the width (W) of the 2-D basin) and experiments where basin rim (R) and background slope (BS) are varied. Figure 2 summarizes the experiments conducted. Topography for the control case (CON) is intended to represent a cross-sectional slice through Arizona's Meteor Crater, aligned with the regional terrain gradient (i.e., approximately southwest-northeast). The model topography features a basin width (depth) of 1200 (160) m, a rim rising approximately 35 m above the surrounding plains, and a 2% background slope upstream of the basin. The reader should note that the actual terrain north and east of Meteor crater is not flat (Figure 1a), as is assumed in all experiments in this study. However, since the actual terrain slopes downward toward lower elevations north and east of Meteor Crater, the impact of such a

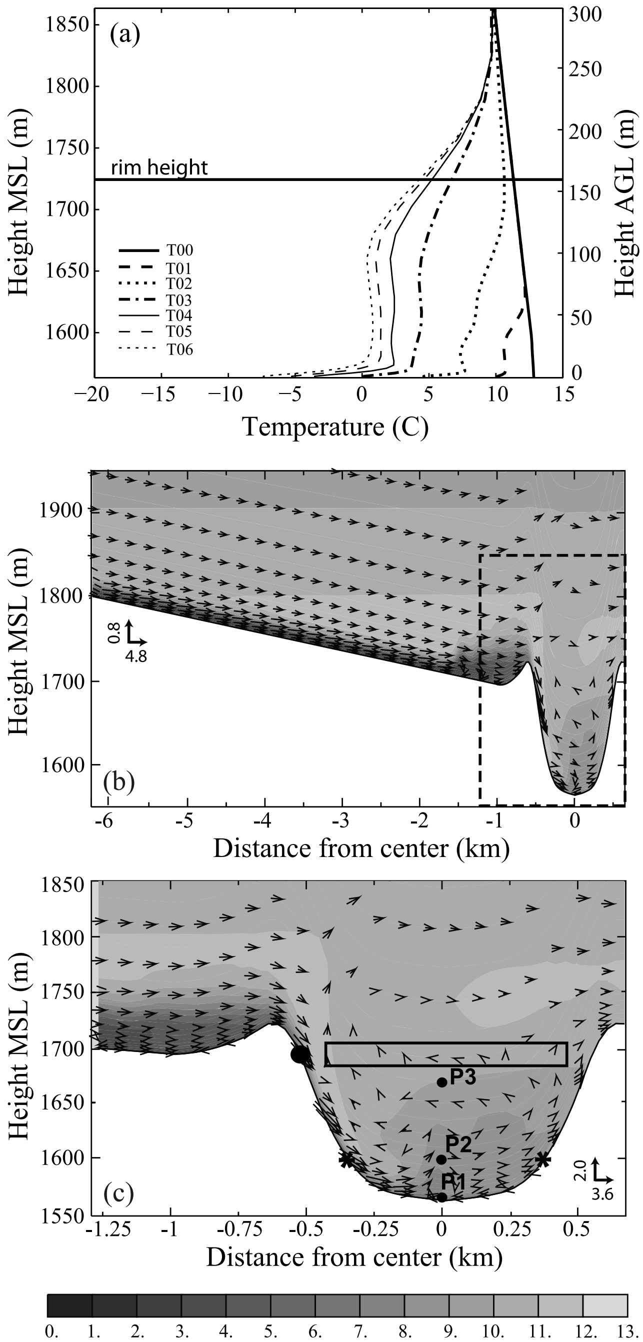

Figure 3. Analysis of case CON. (a) Hourly vertical profiles of air temperature (C) at basin center for the period T00-T06 (0–6 h after initialization) and (b and c) vertical cross sections of air temperature (shaded; C) and wind vectors (m s^{-1}), at time T02. Figures 3b and 3c depict regional and basin-scale view, with the latter zoomed into the basin for greater clarity of features; see dashed outline in Figure 3b. In Figure 3c, the three small circles (labeled P1, P2, P3) correspond to the points used for the thermodynamic budget time series in Figure 4, the large circle and rectangle indicate the point location and averaging area used to compute the time series in Figure 5, and the asterisks indicate the locations used for the WL and EL profiles in Figure 6.

simplification on the basin atmosphere is expected to be minimal. For convenience, we utilize a naming convection in which one or more prefixes (where R is rim, NR is no rim, W is width, and BS is background slope) are combined with a numeral suffix, which connotes either the width of the basin (e.g., 2400 m) or the background slope of the upstream terrain (e.g., 2%). In the first set of sensitivity experiments (RW1200 (i.e., CON), RW2400, RW4800, RW9600; Figure 2a) the terrain upstream of the basin is fixed in order to examine the impact of basin width on basin cooling and thermal structure. In the second set of experiments (RBS2 (i.e., CON), NRBS2, RBS0, NRBS0; Figure 2b), the width of the basin is fixed at 1200 m and the effect of the rim and upstream background slope on basin cooling processes and thermal structure is considered.

3. Results and Discussion

3.1. Control Case

[13] We begin by examining the control case (CON) in order to first assess the ability of the model to reproduce the phenomena observed during METCRAX and, second, evaluate the nocturnal cooling process inside the basin. Figure 3 illustrates the thermal structure simulated in CON, with the basin center temperature profiles in Figure 3a indicating that ARPS is able to reproduce the thermal structure observed on quiescent nights during METCRAX (compare Figures 1c and 3a). Within the first 3 h of the simulation (T00-T03, where "03" refers to the hour after initialization), a three-layer structure develops inside the basin, including an isothermal layer and a strong surface-based inversion (Figure 3a). Outside the basin, a cold air drainage flow is simulated (Figure 3b), with peak along-slope wind speeds of 5–6 m s^{-1} developing by T03 (not shown), with the jet maxima located approximately 15 m AGL. Such details agree well with observations on quiescent nights during METCRAX [*Savage et al.*, 2008]. As also seen in Figure 3b, cold air pooling is simulated within an approximately 50-m-deep layer upstream of the basin rim, extending as far as 1 km upstream. The cold air upstream of the basin is seen to surmount the rim and drain down the sidewalls toward the floor of the basin (Figure 3c), while radiative loss from the basin floor promotes development of a shallow temperature inversion across the lowest 10–15 m of the basin (Figure 3a).

[14] The time series of thermodynamic budget terms presented in Figure 4 (see Appendix A for details of budget) confirm that the cooling at the surface within the basin center is not a result of advection but rather cooling of the underlying ground surface. Figure 4a indicates that the primary cooling mechanism for the formation of the surface inversion is vertical turbulent mixing (MIX_V). The air in immediate contact with the ground cools due to the dominance of the outgoing longwave radiation flux (not shown), and the chilled air is mixed upward via turbulent flux divergence (the vertical component is parameterized in ARPS as $\frac{\partial}{\partial z}(\overline{\rho} K_H \frac{\partial \theta}{\partial z})$, where $\overline{\rho}$ is base state density, K_H is eddy diffusivity and θ is potential temperature). The total cooling rate is much larger at the surface than in the interior of the basin (compare Figure 4a to Figures 4b and 4c), consistent with the development of the strong surface inversion. The dominance of vertical turbulent mixing is

restricted to the lowest 10 m of the basin, above which cooling due to turbulent mixing is negligible (Figures 4b and 4c).

[15] Regarding basin cooling processes, the cross sections of temperature also suggest the means by which the basin-wide cooling evident in the vertical profiles (Figure 3a) is achieved. Broad upward motion inside the basin, a consequence of mass conservation, cools the basin atmosphere away from the floor and sidewalls via adiabatic cooling. From the cross sections (Figures 3b and 3c), it can be inferred that the cold air pool inside the basin is deepening as a result of upward motion. Analysis of ARPS thermodynamic budget forcing terms confirms this finding (Figures 4b and 4c). Of importance in Figure 4 is the period of peak cooling at points away from the basin floor (P2 and P3) between T02 and T03; the cooling is dominated by vertical advection at point P2 and horizontal advection at P3. The slightly larger total cooling rate at point P2 (Figure 4b) is consistent with the trends in the temperature profiles, as well as the development of the isothermal layer (Figure 3a). The horizontal advection at P3 is not entirely surprising considering the predominance of horizontal air motion in the upper 1/3 of the basin (Figure 3c). *Haiden et al.* [2011] cite adiabatic cooling as a process key to the formation of the isothermal layer. As they point out, in the absence of other thermodynamic processes, adiabatic cooling in the basin will produce a layer of neutral buoyancy above the level of neutral buoyancy of the inflow air, i.e., above the surface-based inversion.

[16] An additional factor related to basin cooling identified by *Whiteman et al.* [2010] and *Haiden et al.* [2011] is the continuous cooling of the air upstream of the basin during the overnight. As seen in the time series of basin inflow potential temperature seen in Figure 5a, the phenomenon is also present in the ARPS simulations. This mechanism has been shown by *Haiden et al.* [2011] to stabilize the layer above the surface-based inversion as progressively colder air enters the basin and drains toward the bottom of the basin; such a process has been described by *Haiden et al.* [2011] as a "filling-up" mode. In the absence of this mechanism, neutral stratification would result due to the dominance of the abiabatic cooling process. Thus the presence of the isothermal layer in our simulations, and the identification of the two competing basin thermodynamic processes, appear to support the findings of *Haiden et al.* [2011] regarding the development of the isothermal layer. It is worth noting that the strengthening of the cold air pool at the bottom of the basin has been shown to lead to a slowing down of sidewall flows due to a reduction of the negative buoyancy of air parcels flowing down the sidewall [*Fleagle*, 1950; *McNider*, 1982]. Although there is evidence of such a process occurring in the present simulations (e.g., U_{IN} in Figure 5b), analysis of the effect of this secondary process on sidewall flow and basin cooling is left to future work.

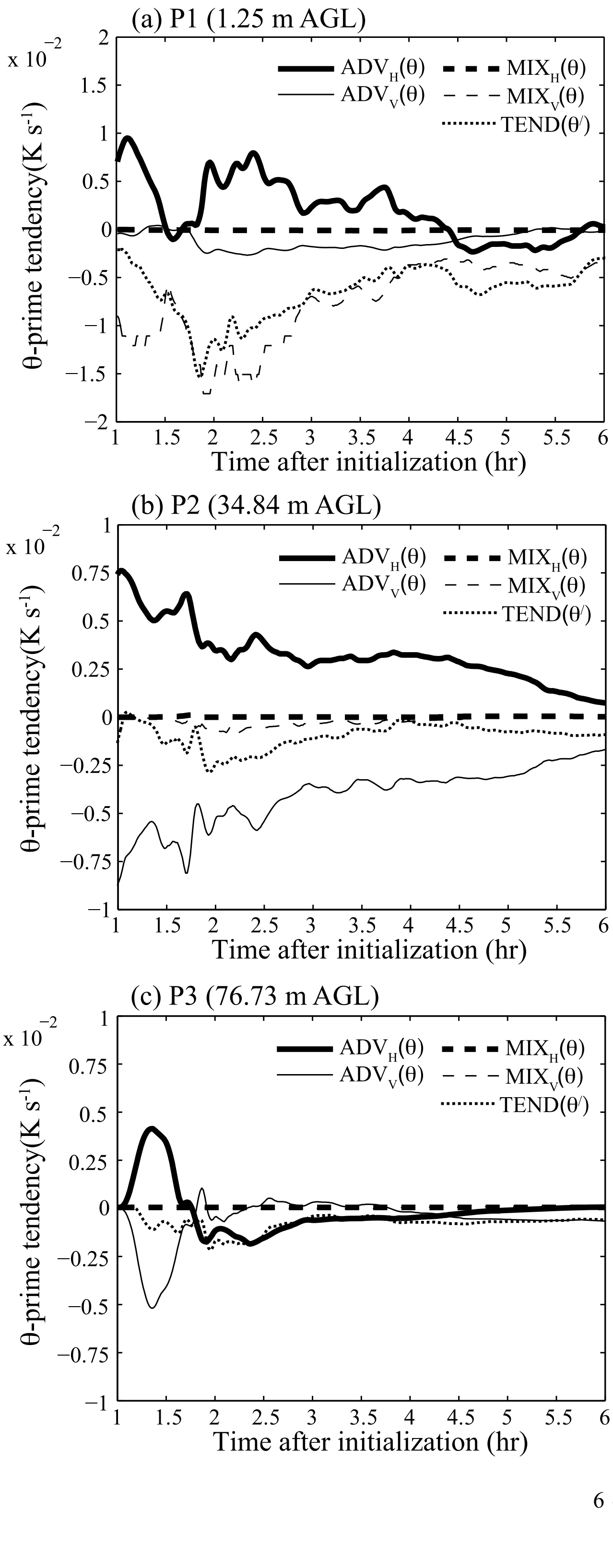

Figure 4. Time series of thermodynamic equation forcing terms, at points (a) P1, (b) P2, and (c) P3, for case CON. See Figure 3c for the location of the points inside the basin. The terms are labeled as follows: MIX_H and MIX_V are horizontal and vertical turbulent mixing of potential temperature, ADV_H and ADV_V are horizontal and vertical advection of potential temperature, and *TEND* is the sum of the four terms. Note that radiation flux divergence (RAD) is omitted from the figure due to the small magnitude of the term, compared to advection and mixing. The time series displayed are nine-point averages, with the central point located at the basin center. Note the change in *y* axis range and tick mark intervals between Figure 4a and Figures 4b–4c. See Appendix A for a detailed description of the terms.

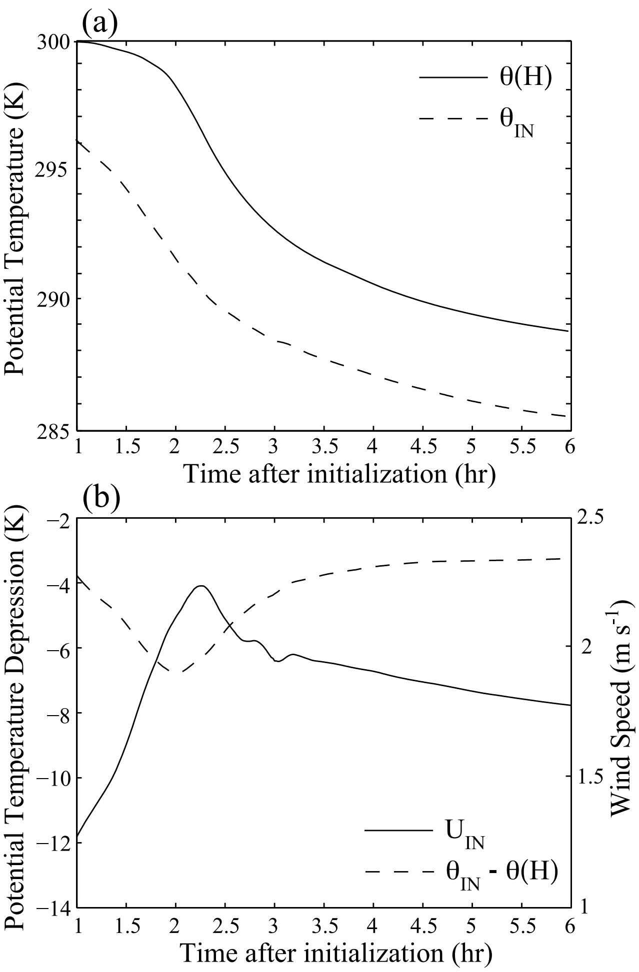

Figure 5. Time series of (a) θ_{IN}, potential temperature of inflow layer air, and $\theta(H)$, average potential temperature of air at top of basin (K), and (b) ($\theta_{IN} - \theta(H)$), inflow potential temperature depression (K), and U_{IN}, inflow wind speed (m s^{-1}). All time series displayed are from case CON. Inflow potential temperature depression is defined as the difference in potential temperature between the inflow layer air and the average value at the top of the basin (see Figure 3c for area used to compute average). Inflow values are surface values at the westernmost point inside the basin, (see Figure 3c for location of point). The components in Figure 5b are used to compute an intrusion cooling rate (ICR), defined in equation (2), and discussed in section 3.2.

[17] A third basin cooling process considered by *Whiteman et al.* [2010] and *Haiden et al.* [2011] is detrainment cooling. The mechanism, proposed to play a role in the formation of the isothermal layer observed during METCRAX, suggests that cold air pouring into the basin flows down the sidewall slope, detrains from the layer immediately along the sidewall, and is mixed laterally across the basin, possibly via breaking Kelvin-Helmholtz waves. In our simulations, however, the tongue of warm air seen in Figure 3c in the western portion of the basin, a feature also identified in METCRAX observations (not shown), suggests that basin cooling due solely to detrainment is likely small in magnitude. Cold air that detrains from the inflow layer along the sidewall would have difficulty mixing across the basin due to the intervening warm tongue. Interestingly, the analytical model developed by *Haiden et al.* [2011] has been shown to produce an isothermal layer even when basin cooling occurs entirely through adiabatic rising motion and the detrainment process is absent. It is important, however, to emphasize that we are unable, from our limited number of 2-D numerical simulations, to eliminate the possibility of detrainment cooling playing an important role in a fully three-dimensional basin such as Meteor Crater. In summary, while uncertainty may exist regarding precisely how basin cooling is achieved, whether through a combination of detrainment and adiabatic motion or predominately through adiabatic motion, consensus does exist regarding the important role of cold air intrusion in the basin cooling process and the isothermal layer development.

[18] It is important to mention the possible impact of turbulent mixing near the western lower sidewall on basin thermal structure, as has been cited in prior studies of katabatic flows [e.g., *McNider and Pielke*, 1984]. As indicated by the wind vectors in Figure 3c, strong wind shear exists immediately above the western lower sidewall, coincident with a region of decreased static stability (as compared to further west along the sidewall). A region of substantial turbulent kinetic energy [O(0.5 m^2 s^{-2})] develops in this area (Figure 6a) but is restricted to the western half of the basin (compare Figures 6a–6c). *McNider and Pielke* [1984], in a series of 2-D numerical simulations of valley flows, found that a weak return (upslope) flow atop the drainage flow layer produced cold air advection above the surface inversion, weakening static stability and promoting mixing in the presence of vertical wind shear. Although such a process appears to exist in CON, it is important to point out that such a mechanism, restricted to the western half of the basin, is unable to explain the formation of the near-homogeneous isothermal layer observed and simulated across the entire basin.

[19] Before proceeding, it is worth briefly discussing several limitations of the 2-D model design. The lack of a third dimension implies that the blocking effect of the rim on the regional-scale drainage flow is underestimated. The limited blocking is evidenced in the peaked nature of the basin cooling rate deduced from the vertical profiles in Figure 3a; an analysis of METCRAX observations suggests that the 2-D simulations overestimate peak cooling rate and also imply that the cooling in reality is more equally distributed throughout the night. As a result of exaggerated cold air intrusion rates, the 2-D model tends to exaggerate the compensating upward motion and associated adiabatic cooling. An additional shortcoming of the 2-D model design is the inability of the model to reproduce the topographic convergence of intruding winds that surmount the rim. The lack of topographic convergence will impact the magnitude of the compensating adiabatic motion in the basin. Additionally, with regards to the simulation of turbulence, the direction of the energy cascade is known to be different for 2-D and 3-D turbulence [*Tennekes*, 1978]. The nonnegligible values of turbulent kinetic energy seen in Figure 6 suggests that caution must be exercised when extrapolating the findings of this 2-D modeling study to 3-D real-world basins. In spite of these model limitations, the qualitative similarity between the atmosphere observed inside Meteor Crater and over the surrounding terrain during METCRAX and that of

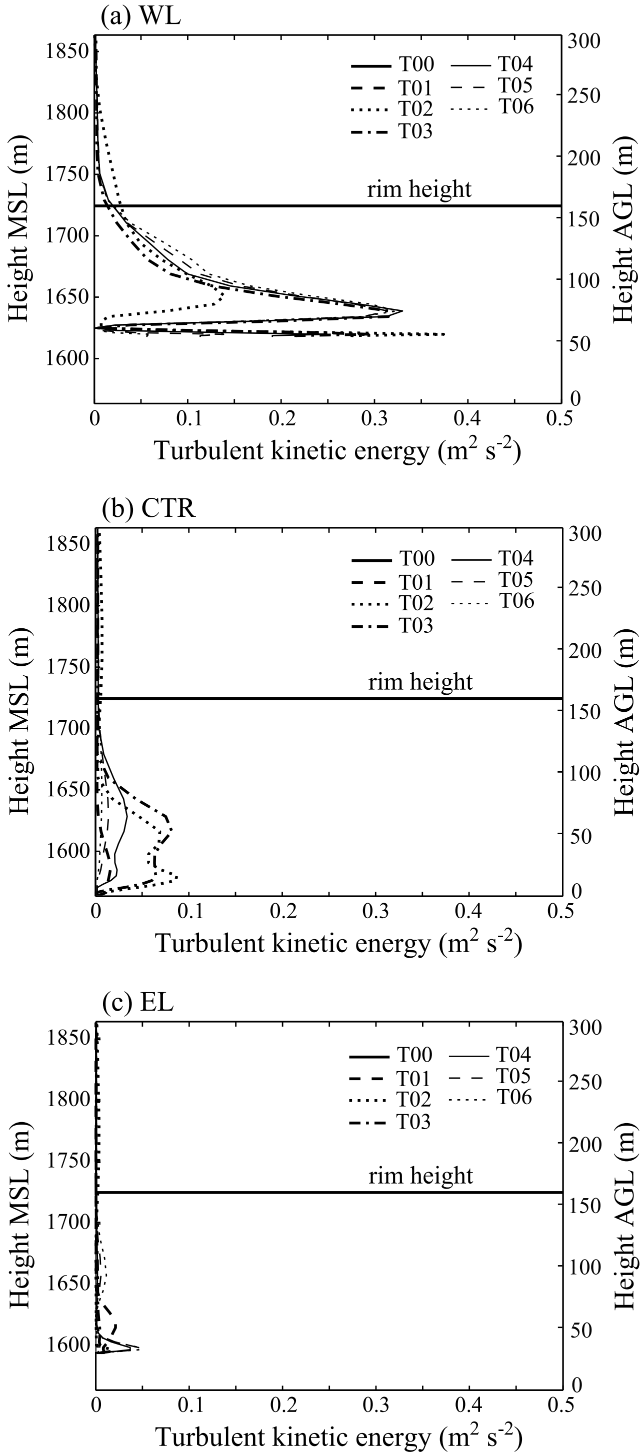

Figure 6. Vertical profiles of turbulent kinetic energy at point (a) WL, (b) CTR, and (c) EL. Point WL is located along the lower western sidewall, approximately 360 m west of point CTR, and point EL is located approximately 360 m east of point CTR (see Figure 3c for locations of points). Note that points WL, CTR, and EL do not correspond exactly to the tethersonde sites WEST, CENTER, and EAST in Figure 1b. Figures 6a–6c are from case CON.

case CON lends support for the use of 2-D experiments in clarifying the role of specific parameters (e.g., basin width) on the basin cooling process.

3.2. Basin Width Experiments

[20] With satisfactory reproduction of the salient features of the crater atmosphere observed on quiescent nights during the METCRAX experiment, discussion now proceeds to examination of the role of various factors (e.g., basin size, basin rim) in basin cooling and development of the three-layer thermal structure. Examining the impact of basin width first, it can be seen in Figure 7 that robust systematic changes in thermal structure are evident in experiments in which basin width is increased. Several aspects of the basin center temperature profiles (Figure 7) are particularly noteworthy. First, the length of time during the evening in which only a surface inversion is present (and the isothermal layer is absent) increases as basin width increases. For CON, this period of surface-dominated cooling is less than an hour (Figure 3a), but increases to at least 1 h for RW2400 and to about 2 h for RW9600. Second, comparing the temperature profiles at time T06 to the initial state, the net amount of basin cooling is found to decrease as basin width increases, although surface temperatures cool between T00 and T06 by approximately the same amount in each case (20–21 C). Given a finite amount of cold air intruding into the basin, a larger basin width implies a greater amount of dilution and thus weaker basin-wide cooling. Last, it is evident that the static stability of the basin atmosphere, once the surface cooling phase ends, is increasingly stable as basin width is increased. For the RW9600 experiment, with a 9.6 km basin width, this yields only a shallow near-isothermal layer. Such changes are consistent with the general expectation that as a basin becomes more and more broad, nocturnal cooling will to an increasing degree resemble cooling over flat, open terrain. In other words, the cold air intrusion process, away from the basin wall, becomes less relevant to nocturnal cooling as basin size increases.

[21] To further elucidate the sensitivity of nocturnal cooling to basin size, basin-average cooling rate (BCR) has been computed for CON and each of the basin width experiments, according to

$$BCR = \left\{ \frac{\sum_{i=1}^{N} \left[\left(\frac{\partial T}{\partial t}\right)_i * (A)_i \right]}{(A)_{basin}} \right\} = \left\{ \frac{\sum_{i=1}^{N} \left[\left(\frac{\partial T}{\partial t}\right)_i * (A)_i \right]}{\sum_{i=1}^{N} (A)_i} \right\} \quad (1)$$

where T is the air temperature of the ith 2-D grid cell inside the basin, $(A)_i$ is the area of the ith 2-D grid cell, and $(A)_{basin}$ is the cross-sectional area of the basin. Note that due to the stretched nature of the vertical grid levels, the area of the 2-D grid cells varies across the basin. See Figure 2 for an illustration of the basin cross-sectional area for each experiment. It is evident from the BCR time series presented in Figure 8a that basin-average cooling decreases as basin width is increased, consistent with conclusions drawn from the basin center temperature profiles (Figure 7). A second feature of note in the BCR time series is the increasing delay in the time of peak cooling, from approximately 2.25 h in CON to about 3.25 h in RW9600. Basin average cooling reaches zenith following the surface-based cooling phase noted in Figure 7 and then gradually decreases thereafter as

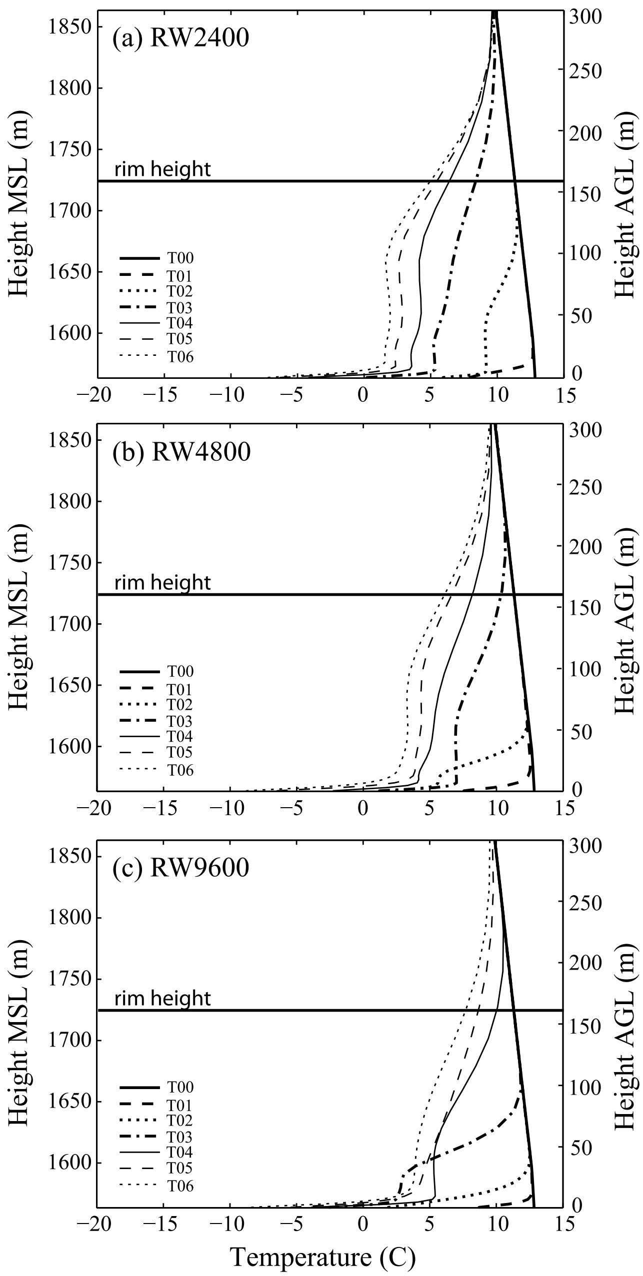

Figure 7. Same as Figure 3a but for the basin width cases (a) RW2400, (b) RW4800, and (c) RW9600.

the difference in potential temperature between the inflow air stream and the average temperature of the air at the top of the basin decreases (Figure 5b). The resultant decrease in negative buoyancy of the inflow air stream can be attributed to the fact that the basin atmosphere cools at a faster rate than that of the incoming air (Figure 5a); as a consequence the regional drainage flow is deflected over the basin to an increasing degree as the night progresses.

[22] In order to better quantify the impact of cold air intrusion on the basin cooling, an intrusion cooling rate (ICR), normalized by basin area, is computed as

$$ICR = \left\{ \frac{U_{IN} D_{IN} [\theta_{IN} - \theta(H)]}{\sum_{i=1}^{N} (A)_i} \right\} \qquad (2)$$

where U_{IN} and D_{IN} are inflow wind speed and the width of the inflow layer along the sidewall, respectively, and θ_{IN} and θ (H) are potential temperature of the inflow layer and ambient potential temperature at the top of the basin, respectively. Equation (2) is based on equation (2) of *Haiden et al.* [2011] and represents an estimate of the amount of basin cooling attributable to intrusion of cold air from outside the basin, normalized by basin area. This cooling estimate accounts for all intrusion cooling processes (e.g., detrainment, adiabatic cooling). In interpreting Figure 8b, we are most interested in the sensitivity of normalized ICR to basin width and less interested in the actual magnitude of ICR. It should be noted that nonnormalized ICR increases with increasing basin width (not shown), through the θ (H) term in equation (2), since basin average cooling weakens with increasing basin size (see Figure 8a or Figure 7). The decreasing magnitude of normalized ICR with increasing basin width see in Figure 8b is expected due to the normalization of ICR by basin area.

[23] Before proceeding, we must emphasize that ICR is an estimate of the amount of basin cooling resulting from the cold air intrusion process. Error in the computation of any of the parameters that make up ICR (e.g., error that results from computing U_{IN} as the surface value at the westernmost point inside the basin) can produce an ICR that is smaller or larger than reality. It is important to note from Figure 8b that while ICR exceeds BCR throughout the CON case time series, the opposite is the case for the largest two basins considered. These differences result from the fact that ICR is an estimate. ICR overestimates basin cooling for the smallest basin (CON) and underestimates basin cooling for the larger basins (RW4800 and RW9600). We reiterate the point that ICR is compared to BCR here to qualitatively evaluate the relationship between basin cooling and cooling due to the intrusion process.

[24] Examining Figure 8b, there is a notable correspondence of the time of peak ICR to that of BCR (compare Figures 8a and 8b), confirming that intrusion of cold air into the basin from the surrounding region is the main source of the basin cooling seen in Figure 3a and Figure 7. Comparing the ICR time series in Figure 8b to the ICR component time series in Figure 5b, it is clear that the peak in basin cooling is due to both a peak in inflow wind speed and a peak in the potential temperature depression of the inflow air. Prior to the peak time, the drainage flow outside of the basin has not yet reached maturity, while after the peak time, the basin top average temperature begins to cool more rapidly than the inflow air such that the inflow air becomes less negatively buoyant. Thus the rate of intrusion cooling peaks and then wanes through the remainder of the simulation. Last, note that a peak in intrusion cooling rate also corresponds to a peak in upward motion and adiabatic cooling rate, as the inflow mass flux (i.e., $U_{IN}D_{IN}$ in equation (2)) is compensated for by upward motion inside the basin (not shown).

3.3. Rim and Background Slope Experiments

[25] Having addressed the impact of basin width on nocturnal basin cooling, we now turn our attention to the question of how the basin rim and gentle upstream terrain slope impact the nocturnal cooling process inside Arizona's Meteor Crater. More specifically, we wish to understand which aspects of the terrain surrounding the basin are critical

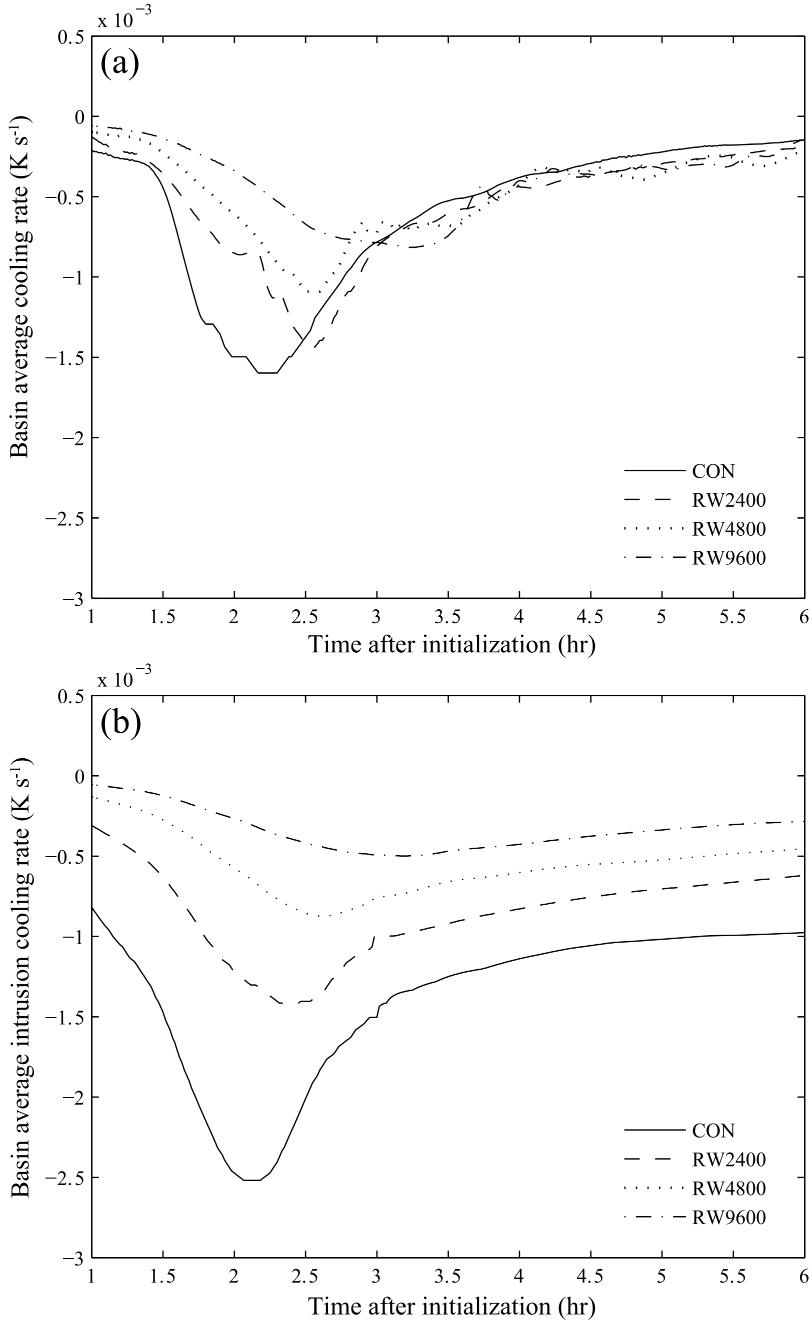

Figure 8. Time series of basin-average (a) computed cooling rate (BCR; K s^{-1}) and (b) estimated intrusion cooling rate (ICR; K s^{-1}), for the basin width experiments. The intrusion cooling rate calculation is based on work by *Haiden et al.* [2011]; see text for further details. The first hour of the simulation is omitted.

to the cooling process and development of the isothermal layer inside the basin. Prior research has suggested that the gentle terrain slope as well as the basin rim play important roles in the basin cooling process and isothermal layer development [*Whiteman et al.*, 2010; *Haiden et al.*, 2011], and it is these claims which we intend to evaluate here. Vertical profiles of temperature at basin center do in fact attest to the important effects of the surrounding terrain on nocturnal cooling inside the basin (Figure 9). Addressing rim impacts first, however, it can be seen in a comparison of CON (Figure 3a) and NRBS2 (Figure 9a) that neither basin cooling nor the three-layer thermal structure are particularly sensitive to the presence or absence of the rim. The depth of the isothermal layer in NRBS2 is approximately 25 m less deep, though this is consistent with the shallower basin in the NRBS2 case (see terrain profile in Figure 2b). Comparison of the vertical cross section of temperature at time T02 for case NRBS2 (Figure 10b) to CON (Figure 3b) further illustrates the limited sensitivity of basin cooling to the presence of the rim. Overall, basin cooling is delayed

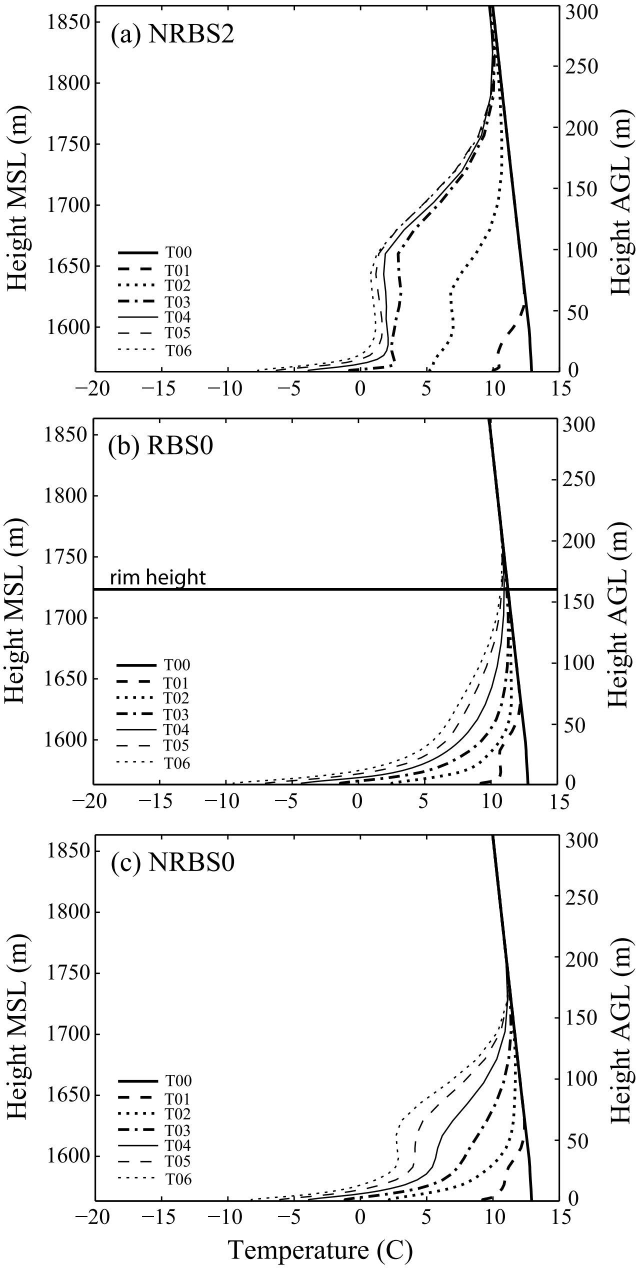

Figure 9. Same as Figure 7 but for the rim and background slope experiments.

and is somewhat weaker in magnitude in the simulation with the rim, a finding that is corroborated by the BCR time series in Figure 11. However, it should be emphasized that our simulations strongly suggest that development of the isothermal layer is not dependent on the presence of the rim.

[26] In contrast, removal of the gentle upstream slope and thus cold air drainage flow yields significant changes to basin cooling. Much weaker cooling is noted away from the basin floor, regardless of the rim presence (Figure 11), and the isothermal layer is eliminated altogether in case RBS0 (compare Figure 3a to Figures 9a and 9b). Removal of the upstream terrain slope yields a basin that is effectively isolated from the surrounding terrain, a state that is exacerbated by the presence of the rim surrounding the basin in case RSB0. Examination of the vertical cross section of temperature for the RBS0 case confirms that cold air upstream is unable to surmount the rim and intrude into the basin (Figure 10d). However, cooling of the sidewall slopes due to radiative loss leads to development of a weak in situ drainage flow that contributes to cold pool development at the bottom of the basin (not shown). Additional tests with an intermediate background slope of 1% have been conducted indicating that a background slope as weak as 1% can yield an isothermal layer, with or without a rim (not shown). However, as evidenced by case NRBS0, an isothermal layer can develop even without a regional scale drainage flow, as long as cold air over the surrounding terrain is able to intrude into the basin (Figure 10f). Future work will further explore the combined effects of background slope and rim height on basin cooling, as well as extend the current work to include 3-D simulations.

3.4. Generality of Findings

[27] The prevalence of regional-scale cold air downslope flows at night at Arizona's Meteor Crater [*Savage et al.*, 2008], and thus the availability of cold air to intrude into the basin, suggests that the three-layer structure described by *Whiteman et al.* [2008] is not an isolated occurrence there. In fact, *Savage et al.* [2008] found that southwesterly downslope flow was present at night over the plains surrounding Meteor Crater more than 50% of the time during October 2006, most commonly under quiescent synoptic conditions. Climatic studies have shown that ridges of high pressure are present in the southwestern United States on more than 70% of the days during the summer and early autumn [*Wang and Angell*, 1999]; stable, calm conditions have been shown to be highly favorable for development of regional-scale terrain-induced circulations. Our results indicate a strong dependence of isothermal layer development on the presence of the regional-scale drainage flow. Thus we expect that the mechanism is probably active on most nights with quiescent conditions, that is, without the influence of broader-scale disturbances such as upper-level troughs or fronts. Further, even on nights where large-scale disturbances disrupt the regional-scale drainage flow, the three-layer structure may be present during at least part of the overnight when regional-scale flow is able to develop [*Whiteman et al.*, 2010]. Last, although the isothermal layer phenomenon was first documented in Meteor Crater, similar boundary layer structure is expected to occur in other basins in the western United States and other mountainous regions of the world.

4. Summary and Conclusions

[28] Idealized 2-D simulations performed with the ARPS model reproduced the key features of the temperature evolution observed inside Arizona's Meteor Crater on quiescent nights during the 2006 METCRAX field campaign. Two aspects of the observed crater atmosphere were investigated: a quasi steady-state three-layer temperature structure, including an isothermal layer away from the basin floor, and the intrusion of a regional-scale cold air drainage flow into the basin. In general, the two-dimensional numerical simulations were able to reproduce the salient features of the nocturnal boundary layer inside Meteor Crater. A series of

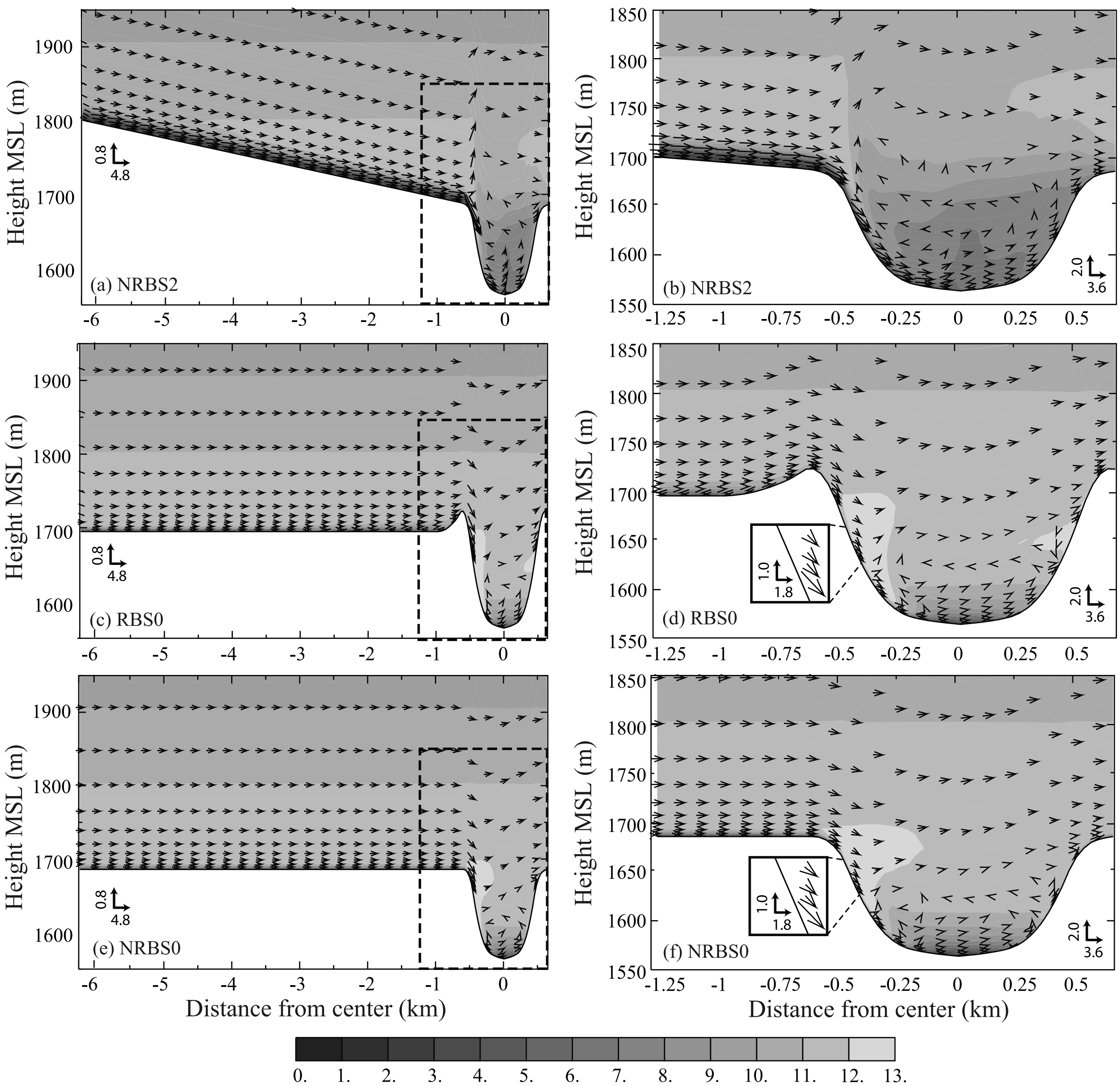

Figure 10. Vertical cross sections of air temperature (shaded; C) and wind vectors (m s^{-1}) for the rim and background slope cases (a, b) NRBS2, (c, d) RBS0, and (e, f) NRBS0, at time T02. Regional view (Figures 10a, 10c, and 10e) and zoomed into the basin for greater clarity (Figures 10b, 10d, and 10f); see dashed outline. A vector key is provided; note difference in vector scales. To improve the visualization of weak katabatic flow in cases RBS0 and NRBS0, insets are provided in the lower left portion of Figures 10d and 10f which display wind vectors along the western sidewall scaled by 200%; see vector key.

experiments were then conducted in order to examine the sensitivity of thermal structure inside the basin to upstream terrain slope, basin width, and the presence or absence of a rim surrounding the basin. A summary of the model results is presented in Figure 12.

[29] In the case of Meteor Crater (Figure 12a), cooling of the upstream gently sloped terrain leads to the development of a cold air drainage flow. While cold air pools upstream of the rim surrounding the basin, a portion of the drainage flow is able to surmount the rim and enter into the basin since the drainage flow is colder than the air inside the basin and therefore negatively buoyant. The mass flux into the basin is compensated for by upward motion inside the basin; the combination of increasingly cold air draining into the basin (a stabilizing process), and the adiabatic lift (a destabilizing process) yields the isothermal layer observed during METCRAX, consistent with *Haiden et al.* [2011]. Meanwhile, radiative loss at the basin floor leads to the development of a strong surface inversion beneath the isothermal layer.

[30] In the case of a large basin of O(10 km) in diameter (Figure 12b), the cold air intrusion process and strong sur-

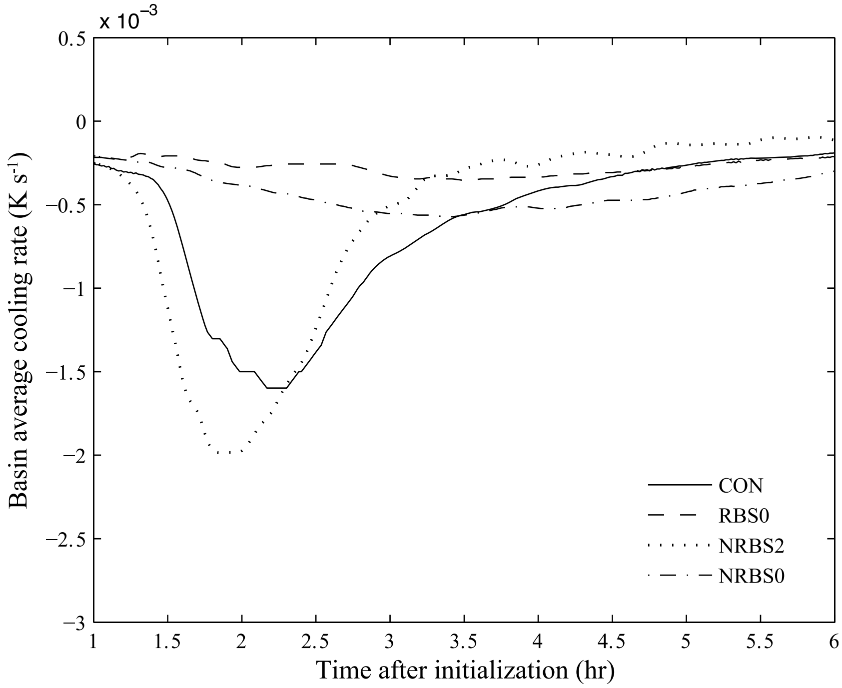

Figure 11. Same as Figure 8a but for the rim and background slope experiments.

face based radiative loss remain, but the much larger basin volume yields greater dilution of the cold air intruding into the basin and a weaker adiabatic response. Thus rather than an isothermal layer, a weak inversion develops inside the basin away from the floor. This is consistent with the expectation that as a basin becomes wider, the nocturnal cooling process will to an increasing degree resemble cooling over flat, open terrain. In other words, the cold air intrusion process, away from the basin sidewall, becomes less relevant to nocturnal cooling as basin size increases.

[31] In the case of a basin with the same dimensions as Meteor Crater, but with zero upstream terrain slope (Figure 12c), the influence of the surrounding terrain on basin cooling is negligible. Cooling of the basin sidewall slopes leads to the development of weak sidewall downslope flow, and cooling of the basin, while radiative loss at the basin floor yields a strong surface inversion. The relative weakness of the adiabatic cooling inside the basin precludes development of an isothermal layer. In the sense that intrusion of cold air into the basin (and compensating adiabatic lift) plays a minimal role in basin cooling, large basins exposed to the effects of a regional drainage flow and isolated small basins without any regional drainage flow are similar. In the case of the large basin exposed to a regional drainage flow, the large volume implies that the compensating vertical motion will be rather weak. For a small, isolated basin without regional drainage flow, the lack of cold air intrusion from outside the basin means that cooling away from the basin sidewalls and floors will be minimal. Both types of basins lack the proper basin and regional-scale terrain geometry needed for development of an isothermal layer. However, the presence of a rim surrounding the basin is not a prerequisite for isothermal layer development, as the results of this study show.

[32] Before concluding, it is important to recall several limitations of this study. First and foremost, the findings are based on two-dimensional simulations. The lack of a third dimension implies that the blocking effect of the rim on the regional-scale drainage flow is underestimated. The limited blocking effect is evidenced in the peaked nature of the basin cooling rate time series; METCRAX observations suggest that the two-dimensional simulations overestimate peak cooling and also imply that the cooling is more equally distributed throughout the night. Additional shortcomings of the 2-D model design include the inability of the model to reproduce the topographic convergence of intruding winds that surmount the rim and the inability of a 2-D model to properly represent the downscale energy cascade. In addition to the two-dimensional limitations, incomplete model radiation physics may affect the interpretation of our results. As the ARPS model only considers the vertical component of radiative fluxes, the effect of the horizontal component of radiative flux from the sidewalls on the temperatures inside the basin are not accounted for.

[33] In spite of such limitations, this study has succeeded in providing valuable insight regarding the development of the three-layer structure inside Arizona's Meteor Crater and the role of cold air intrusion into the basin on the cooling process. However, much work remains, including examining a larger parameter space, extending the simulations to 3-D, and performing additional model budget analysis to more definitively identify the physical processes critical to the unique thermal structure observed inside Meteor Crater. Additional parameters are likely to impact the cooling process and need to be examined in future work, including upstream wind and stability, sidewall slope, rim height, and basin depth. Extension of this work to 3-D will allow for further assessment of the role of blocking in the

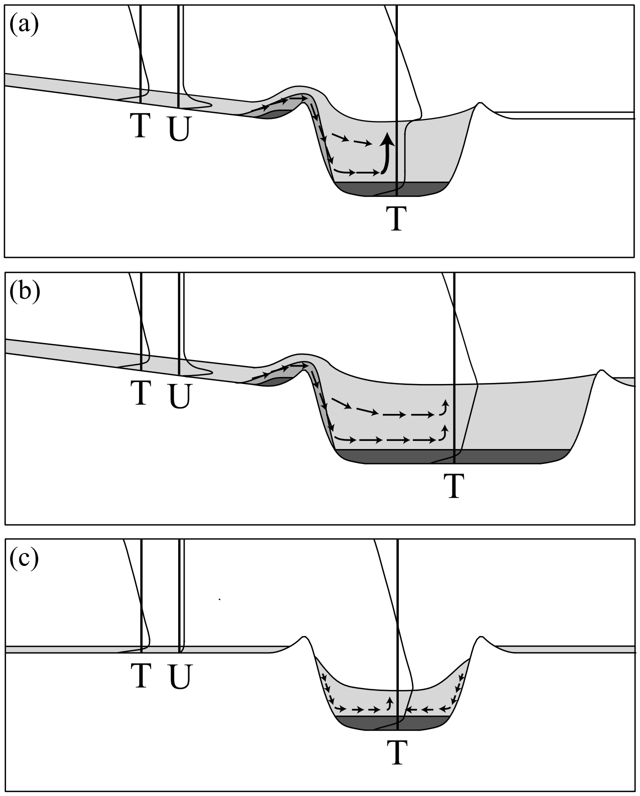

Figure 12. Conceptual model of nocturnal cooling processes for (a) Meteor Crater, (b) large basin of O(10 km) in width, and (c) isolated basin with no upstream terrain slope. Vertical profiles of mean temperature are displayed upstream of the basin and at basin center, and profiles of rim-normal wind component are displayed upstream of the basin. Arrows indicate direction of wind flow in the 2-D cross section, with the thickness of the vertical arrow at basin center indicating the magnitude of the vertical motion. The shading denotes cold air layers, with the darkest shade depicting the locations of the coldest air.

basin cooling process. Along with the important findings of this study, such future work is expected to provide additional insight into how airflow outside of a closed basin can impact the nocturnal boundary layer inside.

Appendix A: Thermodynamic Budget

[34] First, consider the thermodynamic equation in the absence of precipitation processes,

$$\frac{\partial \theta'}{\partial t} = -\overline{\rho} w \frac{\partial \overline{\theta}}{\partial z} - \vec{u} \bullet \nabla \theta' + \nabla \bullet \vec{H} + R \qquad \text{(A1)}$$

where we have neglected in equation (A1) coordinate transformation factors in the ARPS prognostic equations (however, they are included in calculated budget terms). In equation (A1), θ refers to potential temperature, $\overline{()}$ and $()'$ refer to base state (function of height only) and perturbation variables, **u** is the total wind vector, and $\vec{H}$ is the three-dimensional turbulent heat flux. Heat flux is computed in ARPS as $\vec{H} = \overline{\rho} K_H(\nabla \theta)$, where $\overline{\rho}$ is base state density and K_H is the thermal turbulent diffusivity. From left to right in equation (A1), the terms are time rate of change, or tendency, of perturbation potential temperature (TEND), adiabatic warming/cooling (ADAB), advection (ADV), turbulent mixing (MIX), and radiative forcing (RAD). For a full description of the ARPS governing equations, see *Xue et al.* [2000, 2001]. Combining the first two terms on the right-hand side of equation (A1) yields advection of total potential temperature, and delineating between forcing in the horizontal and vertical dimensions yields

$$TEND(\theta') = ADV_H(\theta) + ADV_V(\theta) + MIX_H(\theta) + MIX_V(\theta) + RAD \qquad \text{(A2)}$$

where subscripts H and V correspond to the horizontal and vertical components of forcing, respectively. In this and all subsequent budget analyses, the tendency term is calculated as a residual by summing each of the forcing terms on the right-hand side of equation (A2). A comparison of the residual of equation (A2) and the actual tendency computed from high-frequency model output suggests that the residual provides a reasonable estimation of tendency (not shown).

[35] **Acknowledgments.** We wish to thank Marwan Katurji, Sebastian Hoch, and two anonymous reviewers for their helpful comments and suggestions regarding the manuscript. We also wish to thank the National Center for Atmospheric Research (NCAR) staff for providing equipment, field support, and data processing and the Barringer Crater Corporation and Meteor Crater Enterprises, Inc. for providing basin access during the METCRAX experiment. This research was supported by the U.S. National Science Foundation Physical and Dynamic Meteorology Division (A. Detwiler, Program Manager) through grant 0837860. Any opinions, findings, and conclusions or recommendations expressed are those of the authors and do not necessarily reflect the views of the National Science Foundation. All simulations were performed on the NCAR supercomputer *Bluefire*, managed and operated by the Computational and Information Systems Laboratory (CISL).

References

Barr, S., and M. M. Orgill (1989), Influence of external meteorology on nocturnal valley drainage winds, *J. Appl. Meteorol.*, *28*, 497–517.
Chou, M.-D. (1990), Parameterization for the absorption of solar radiation by O_2 and CO_2 with application to climate studies, *J. Clim.*, *3*, 209–217.
Chou, M.-D. (1992), A solar radiation model for climate studies, *J. Atmos. Sci.*, *49*, 762–772.
Chou, M.-D., and M. J. Suarez (1994), An efficient thermal infrared radiation parameterization for use in general circulation models, *Tech. Memo. 104606*, NASA, Linthicum Heights, Md.
Clements, C. B., C. D. Whiteman, and J. D. Horel (2003), Cold-air-pool structure and evolution in a mountain basin: Peter Sinks, Utah, *J. Appl. Meteorol.*, *42*, 752–768.
Colette, A. G., F. Katopodes Chow, and R. L. Street (2003), A numerical study of inversion-layer breakup and the effects of topographic shading in idealized valleys, *J. Appl. Meteorol.*, *42*, 1255–1272.
Fleagle, R. G. (1950), A theory of air drainage, *J. Meteorol.*, *7*, 227–232.
Fritts, D. C., D. Goldstein, and T. Lund (2010), High-resolution numerical studies of stable boundary layer flows in a closed basin: Evolution of steady and oscillatory flows in an axisymmetric Arizona Meteor Crater, *J. Geophys. Res.*, *115*, D18109, doi:10.1029/2009JD013359.
Geiger, R. (1965), *The Climate Near the Ground*, Harvard Univ. Press, Cambridge, Mass.
Gustavsson, T., M. Karlsson, J. Bogren, and S. Lindqvist (1998), Development of temperature patterns during clear nights, *J. Appl. Meteorol.*, *37*, 559–571.
Haiden, T., C. D. Whiteman, S. W. Hoch, and M. Lehner (2011), A mass-flux model of nocturnal cold air intrusions into a closed basin, *J. Appl. Meteorol. Climatol.*, *50*, 933–943.
LeMone, M. A., K. Ikeda, R. L. Grossman, and M. W. Rottach (2003), Horizontal variability of 2-m temperature at night during CASES-97, *J. Atmos. Sci.*, *60*, 2431–2449.
Mahrt, L., D. Vickers, R. Nakamura, M. R. Soler, J. Sun, S. Burns, and D. H. Lenschow (2001), Shallow drainage flows, *Boundary Layer Meteorol.*, *101*, 243–260.

McNider, R. T. (1982), A note on velocity fluctuations in drainage flows, *J. Atmos. Sci.*, *39*, 1658–1660.
McNider, R. T., and R. A. Pielke (1984), Numerical simulation of slope and mountain flows, *J. Appl. Meteorol. Climatol.*, *23*, 1441–1453.
Noilhan, J., and S. Planton (1989), A simple parameterization of land surface processes for meteorological models, *Mon. Weather Rev.*, *117*, 536–549.
Pleim, J. E., and A. Xiu (1995), Development and testing of a surface flux and planetary boundary layer model for application in mesoscale models, *J. Appl. Meteorol.*, *34*, 16–32.
Reddy, P. J., D. E. Barbarick, and R. D. Osterburg (1995), Development of a statistical model for forecasting episodes of visibility degradation in the Denver metropolitan area, *J. Appl. Meteorol.*, *34*, 616–625.
Savage, L. C., S. Zhong, W. Yao, W. J. O. Brown, T. W. Horst, and C. D. Whiteman (2008), An observational and numerical study of a regional-scale downslope flow in northern Arizona, *J. Geophys. Res.*, *113*, D14114, doi:10.1029/2007JD009623.
Smith, R. B., et al. (1997), Local and remote effects of mountains on weather: Research needs and opportunities, *Bull. Am. Meteorol. Soc.*, *78*, 877–892.
Steinacker, R., C. D. Whiteman, M. Dorninger, E. Mursch-Radlgruber, K. Baumann, S. Eisenbach, A. M. Holzer, and B. Pospichal (2007), A sinkhole field experiment in the Eastern Alps, *Bull. Am. Meteorol. Soc.*, *88*, 701–716.
Tennekes, H. (1978), Turbulent flow in two and three dimensions, *Bull. Am. Meteorol. Soc.*, *59*, 22–28.
Thompson, B. W. (1986), Small-scale katabatics and cold hollows, *Weather*, *41*, 146–153.
Vosper, S. B., and A. R. Brown (2008), Numerical simulations of sheltering in valleys: The formation of nighttime cold air pools, *Boundary Layer Meteorol.*, *127*, 429–448.
Wang, J. X. L., and J. K. Angell (1999), Air stagnation climatology for the United States (1948–1998), *Tech. Rep. 1*, Air Resour. Lab., NOAA, Washington, D. C.
Whiteman, C. D., T. B. McKee, and J. C. Doran (1996), Boundary layer evolution within a canyonland basin, Part I: Mass, heat and moisture budgets from observations, *J. Appl. Meteorol.*, *35*, 2145–2161.
Whiteman, C. D., S. Zhong, and X. Bian (1999), Wintertime boundary layer structure in the Grand Canyon, *J. Appl. Meteorol.*, *38*, 1084–1102.
Whiteman, C. D., S. Zhong, W. J. Shaw, J. M. Hubbe, X. Bian, and J. Mittelstadt (2001), Cold pools in the Columbia Basin, *Weather Forecasting*, *16*, 432–447.
Whiteman, C. D., et al. (2008), Metcrax 2006 - Meteorological experiments in Arizona's Meteor Crater, *Bull. Am. Meteorol. Soc.*, *89*, 1665–1680.
Whiteman, C. D., S. W. Hoch, M. Lehner, and T. Haiden (2010), Nocturnal cold -air intrusions into a closed basin: Observational evidence and conceptual model, *J. Appl. Meteorol. Climatol.*, *49*, 1894–1905.
Xue, M., K. K. Droegemeier, and V. Wong (2000), The Advanced Regional Prediction System (ARPS) – A multi-scale nonhydrostatic atmosphere simulation and prediction model, Part I: Model dynamics and verification, *Meteorol. Atmos. Phys.*, *75*, 463–485.
Xue, M., K. K. Droegemeier, V. Wong, A. Shapiro, K. Brewster, F. Carr, D. Weber, Y. Liu, and D. Wang (2001), The Advanced Regional Prediction System (ARPS) – A multi-scale nonhydrostatic atmosphere simulation and prediction tool, Part II: Model physics and applications, *Meteorol. Atmos. Phys.*, *76*, 143–165.
Xue, M., D. Wang, J. Gao, K. Brewster, and K. K. Droegemeier (2003), The Advanced Regional Prediction System (ARPS), storm-scale numerical weather prediction and data assimilation, *Meteorol. Atmos. Phys.*, *82*, 139–170.
Yao, W., and S. Zhong (2009), Nocturnal temperature inversions in a small, enclosed basin and their relationship to ambient atmospheric conditions, *Meteorol. Atmos. Phys.*, *103*, 195–210.

M. T. Kiefer and S. Zhong, Department of Geography, Michigan State University, 1407 S. Harrison Road, Room 220, East Lansing, MI 48823, USA. (mtkiefer@msu.edu)